International Journal for Multidisciplinary Research (IJFMR)
E-ISSN: 2582-2160 • Website: www.ijfmr.com • Email: editor@ijfmr.com

PSO-Tuned Sugeno Fuzzy Control of Partial Rotor-Reactance Compensation During Starting of a 5 MW Slip-Ring Induction Motor

Muralidharan Dhandapani[1], Soumyakant Satapathy[2]

[1,2]Electrical and Electronics Engineering, Technical and Administrative Training Institute (TATI), Muscat, Oman

Abstract

High-power wound-rotor induction motors remain useful in oil-and-gas installations because an external liquid resistance starter (LRS) provides controllable starting torque. However, rotor leakage reactance contributes to lagging displacement power factor during acceleration. This paper proposes a particle-swarm-optimised zero-order Sugeno fuzzy supervisor that coordinates LRS electrode travel with bounded rotor-side capacitive reactance cancellation. The physically consistent partial-compensation relation is Ceff = Cres/α, where α = |XC|/XL and $0 < \alpha \leq 0.72$; the capacitor branch is disconnected when α is below the enable threshold, hardware-equivalent capacitance exceeds its ceiling, or independent protection permissives fail. A reproducible fundamental-frequency reduced-order model compares conventional LRS, an independently optimised fixed capacitor, an untuned fuzzy supervisor and the PSO-tuned fuzzy design for a 5 MW, 6.6 kV, four-pole motor. Twelve independently seeded PSO runs provide repeatability evidence. Under combined conductivity, temperature and load stress, mean starting displacement power factor increases from 0.8506 to 0.8662 (+1.84% relative), while mean reactive power decreases by 7.51% relative to conventional LRS and by 4.19% relative to the optimised fixed-capacitor comparator. Peak-current change is +0.28% and LRS dissipated-energy change is +0.36%. A five-level 150-250 mF effective-capacitance screening study and a three-profile re-ranking of the twelve realised PSO candidates quantify hardware-limit and objective-preference sensitivity. The findings are reproducible numerical design-study results; they do not represent measured plant performance, a trained ANFIS, a certified converter design or experimental validation.

Keywords: liquid resistance starter; slip-ring induction motor; rotor reactance compensation; starting power factor; switched capacitor; Sugeno fuzzy control; particle swarm optimisation; oil and gas.

1. Introduction

Large process pumps, compressors, mills, crushers and conveyors can require substantial breakaway torque while operating from networks with finite short-circuit strength. Wound-rotor induction motors provide access to the rotor circuit through slip rings, allowing external resistance to shape starting torque, stator current and acceleration. An electrolytic liquid resistance starter varies effective external resistance through electrode position, electrolyte conductivity and tank temperature [1]-[3].

Conventional LRS schedules primarily manage resistive starting behaviour. They do not directly compensate rotor leakage reactance, which contributes to lagging motor displacement power factor. Rotor-impedance control and rotor-side switched capacitance have established technical antecedents, including laboratory-scale dynamic-capacitor demonstrations [4]-[6], [19]-[23]. Nevertheless, directly translating those concepts to a megawatt-class liquid starter introduces slip-frequency variation, very large apparent capacitance, independent protection requirements, converter stresses and electrolyte-dependent dynamics. The paper investigates whether safely bounded partial rotor-reactance cancellation can improve power factor specifically during motor starting. The proposed control architecture combines a zero-order Sugeno fuzzy supervisor with offline particle swarm optimisation (PSO). This terminology is deliberate: because no neural-network learning, hybrid ANFIS training dataset or trained consequent parameters are demonstrated, the system is not represented as ANFIS [7], [8].

The contributions are: (i) a corrected derivation linking compensation fraction to effective rotor capacitance; (ii) an explicitly defined reduced-order motor, network, electrolyte, actuator and thermal model; (iii) a transparent six-parameter PSO-tuned Sugeno fuzzy supervisor; (iv) a four-controller comparison including an independently optimised fixed-capacitor baseline; (v) repeatability evidence from twelve seeded optimisation runs; (vi) effective-capacitance-ceiling and fully specified objective-preference sensitivity studies; and (vii) a clearly bounded industrial validation roadmap. Claims concern displacement power factor during starting, not continuous-running or whole-plant true power factor.

2. Related Research and Research Gap

2.1 Wound-rotor starting and external rotor impedance

Classical work by Shepherd and Slemon, Ayyadurai and colleagues, Baghouz and Tan, and Sen and Ma established the importance of external rotor impedance, rotor choppers and efficiency-oriented control [19]-[21], [23]. Recent modelling and digital-twin studies show the benefits of identified machine parameters and higher-fidelity representations, while also highlighting the limitations of simplified equivalent circuits [9]-[12]. In an LRS, the resistance-position relationship additionally depends on electrolyte concentration, temperature, conducting geometry and electrode motion; therefore, a timed ramp alone does not guarantee the same electrical trajectory after ageing or process disturbance.

2.2 Dynamic capacitors and rotor-side compensation

Reinert and Parsley investigated rotor-circuit resonance for speed control, and Suciu and colleagues described phase advancement using switched capacitors [5], [6]. Ranjith Kumar, Palaniswami and Manikandan experimentally investigated a laboratory wound-rotor induction motor using a rectified rotor circuit, an H-bridge dynamic capacitor and DSP-generated switching pulses [4]. Their results establish a relevant laboratory precedent, but they neither validate a 5 MW LRS installation nor remove the need for rotor-voltage, current, switching-loss, insulation and hazardous-area design.

A crucial physical distinction is that the reactance of a series capacitor varies inversely with its capacitance. If the desired capacitive reactance is only a fraction of the rotor inductive reactance, the required effective capacitance must exceed the full-resonance capacitance, not fall below it. A controller that uses $C_{eff} = \alpha C_{res}$ while simultaneously modelling $X_{net} = X_L(1-\alpha)$ mixes incompatible definitions. The present work removes that inconsistency.

2.3 Fuzzy supervision, optimisation and stated gap

Fuzzy motor control offers interpretable operating rules, whereas PSO supplies a derivative-free offline method for selecting gains, membership parameters and constraint penalties [7], [8], [13], [22]. A trained adaptive-network fuzzy inference system requires additional network-layer and learning evidence beyond ordinary fuzzy inference. Therefore, the identified gap is not generic 'AI control' but coordinated and correctly parameterised LRS resistance plus safe rotor-reactance cancellation under explicitly modelled conductivity, load and temperature disturbances.

The testable hypothesis is that an offline-optimised Sugeno fuzzy supervisor improves starting displacement power factor and reduces mean reactive demand relative to uncompensated LRS, an optimised fixed-capacitor baseline and an untuned fuzzy controller, while all compensated configurations respect the same maximum reactance-cancellation limit.

3. Proposed Starting Architecture and Corrected Compensation Physics

3.1 Plant topology and operating sequence

The proposed arrangement comprises a 6.6 kV motor bus, a 5 MW wound-rotor induction motor, a three-phase electrolytic starter, a rotor-side dynamic-capacitance converter and an independent rotor-bypass/protection system. The supervisor measures motor speed, stator voltage and current, estimated displacement power factor and bulk electrolyte temperature. Its commands are electrode-position reference and rotor-reactance cancellation factor.

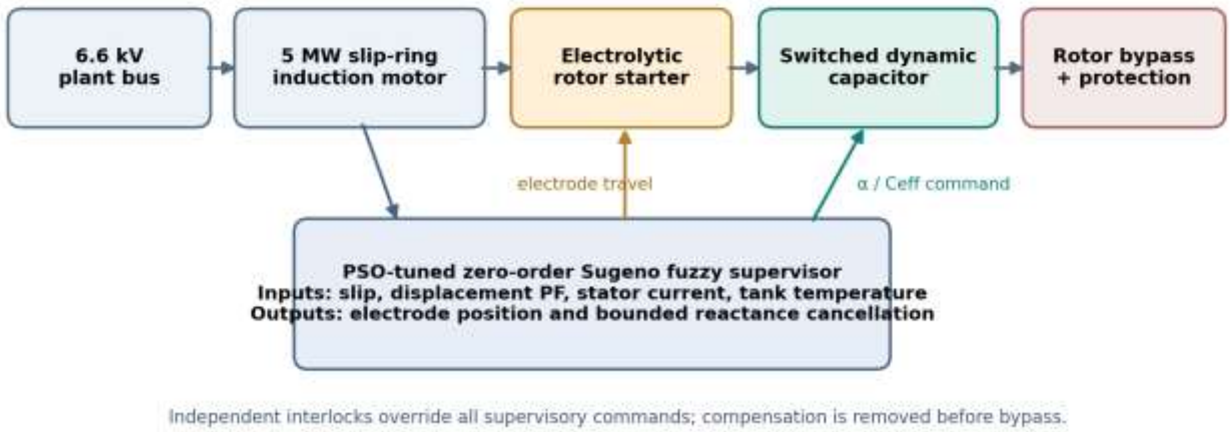

Figure 1. Proposed LRS, dynamic-capacitance and independently protected rotor-bypass architecture.

The operating sequence is: verify tank, actuator and protection permissives; energise the motor with high external rotor resistance; move the electrodes subject to their travel-rate limit; enable compensation only within the approved slip, current, temperature and effective-capacitance window; remove compensation as the bypass region approaches; and close the rotor bypass only after isolation is confirmed. Protection remains independent from the fuzzy supervisor [3], [27], [28].

3.2 Slip frequency, resonance and physically correct partial cancellation

$$n_s = 120f/p, \quad s = (n_s - n_r)/n_s, \quad f_r = sf, \quad \omega_{re} = 2\pi sf \tag{1}$$

$$X^L(s) = \omega_{re}L_r, \quad |X^c(s,C_eff)| = 1/(\omega_{re}C_eff) \tag{2}$$

$$C_{res}(s) = 1/[\omega_{re}^2L_r] = 1/[(2\pi sf)^2L_r] \tag{3}$$

$$\alpha = |X^c|/X^L, \quad 0 < \alpha \leq \alpha_{max} < 1 \tag{4}$$

$$C_eff(s,\alpha) = C_{res}(s)/\alpha, \quad X_{net} = X^L(1 - \alpha) \tag{5}$$

$$m_{res} = 1 - \alpha \geq 0.28 \quad \text{for} \quad \alpha_{max} = 0.72 \tag{6}$$

Equation (5) is the essential correction: reducing the desired capacitive reactance requires a larger capacitance because |XC| is inversely proportional to Ceff. For α = 1, Ceff = Cres and full series resonance occurs; for $\alpha = 0.72$, Ceff = Cres/0.72 and 28% of inductive reactance remains uncompensated. For $\alpha = 0$, the capacitor branch is physically disconnected; assigning a finite capacitor to that state would be incorrect.

Table 1. Corrected slip-frequency capacitance using Ceff = Cres/α.

Slip s	Rotor f (Hz)	Full resonance Cres (µF)	72% cancellation Cres/0.72 (µF)	225 mF ceiling
1.00	50.0	2,621	3,641	Enabled
0.75	37.5	4,660	6,472	Enabled
0.50	25.0	10,485	14,562	Enabled
0.25	12.5	41,939	58,248	Enabled
0.18	9.0	80,900	112,361	Enabled

The tabulated capacitances are stator-referred effective values. They are not procurement-ready physical capacitor ratings. Any practical H-bridge, rectified-rotor or virtual-capacitance topology must be mapped through the actual rotor turns ratio, capacitor voltage, converter duty law, ripple current and stored-energy limits [4], [6].

4. Reproducible Motor, Network, LRS and Thermal Model

4.1 Electrical bases and per-unit equivalent circuit

$\text{Ibase} = P_n/(\sqrt{3}\, V^{LL}\, \eta_n\, PF_n), \quad \text{Sbase} = \sqrt{3}\, V^{LL}\, \text{Ibase}$ (7)

$\text{Zbase} = (V^{LL}/\sqrt{3})/\text{Ibase}, \quad L'_r = X'_2\text{Zbase}/(2\pi f)$ (8)

$Z_r{,}pu = (R'_2{,}pu + R^{LRs}{,}pu)/s + jX'_2{,}pu(1 - \alpha)$ (9)

$Z_m{,}pu = jX_m{,}pu, \quad Zin{,}pu = R_1{,}pu + jX_1{,}pu + (Z_m{,}pu\, Z_r{,}pu)/(Z_m{,}pu + Z_r{,}pu)$ (10)

$I_s{,}pu = Vbus{,}pu/Zin{,}pu, \quad S_{pu} = Vbus{,}pu\, I_s{,}pu^* = P_{pu} + jQ_{pu}$ (11)

$PFdisp = P_{pu}/|S_{pu}|, \quad P(W) = P_{pu}\text{Sbase}, \quad Q(var) = Q_{pu}\text{Sbase}$ (12)

With $\eta_n = 0.96$, rated PF = 0.88, 5 MW rated mechanical output and 6.6 kV line voltage, the resulting line-current base is 517.74 A, apparent-power base is 5.919 MVA, impedance base is 7.3599 Ω and stator-referred rotor leakage inductance is 3.8655 mH. Equation (11) is explicitly per unit; dimensional three-phase power is recovered using Sbase, avoiding ambiguity between phase and line quantities [9], [11], [17], [18].

4.2 Electrolyte conductivity and mechanically limited electrode travel

$\kappa rel(T,c) = \kappa c[1 + \beta T(T - Tref)], \quad \beta T = 0.011\ °C^{-1}, \quad Tref = 35\ °C$ (13)

$R^{LRs}{,}pu(x,T,c) = [Rmin + (Rmax - Rmin)(1 - x)^{1.36}]/\kappa rel$ (14)

$dx/dt = sat[(x^* - x)/\tau a, -vmax, vmax], \quad 0 \le x \le 1$ (15)

Here x = 0 corresponds to maximum modelled starter resistance and x = 1 to minimum resistance. The conductivity law and exponent are transparent design-study assumptions rather than measured commercial-tank characteristics. The supervisor adjusts x* while the actuator enforces a 1.45 s first-order response and 0.062 s^{-1} maximum travel rate.

4.3 Torque, load profile, temperature and weak-network approximation

$T_e{,}pu = |I'_r{,}pu|^2(R'_2{,}pu + R^{LRs}{,}pu)/s, \quad Tbase = Sbase/\omega syn$ (16)

$J\, d\omega_m/dt = Tbase(T_e,pu - T^L,pu) - B\omega_m$ (17)

$P^{LRs}(W) = Sbase|I'_r,pu|^2R^{LRs},pu, \quad dT/dt = P^{LRs}/Cth - (T - Tamb)/\tau cool$ (18)

$Vbus,pu = \max[Vmin, 1 - kg \max(|I_s,pu| - 1,0)]$ (19)

$T^L,pu = kL(0.085 + 0.78\omega_{pu}^2) + \delta_1(t) + \delta_2(t) + 0.020\sin(2\pi\cdot 0.16t)$ (20)

For disturbed scenarios, $\delta_1 = 0.052$ pu from 10 s to 23 s and $\delta_2 = 0.034$ pu from 28 s to 38 s; outside those windows both terms are zero. The sinusoidal disturbance is absent in the nominal scenario. Initial rotor speed is zero, initial electrode position is zero, initial compensation is zero, and initial tank temperature equals ambient temperature plus 1.5 °C. The scalar network model is solved consistently with the current-dependent bus voltage and is not an electromagnetic-transient or harmonic model.

Table 2. Complete assumed motor, starter, network and simulation parameters.

Parameter	Assigned value	Unit / interpretation
Rated output / line voltage	5.0 / 6.6	MW / kV
Frequency / poles / synchronous speed	50 / 4 / 1500	Hz / count / rpm
Rated efficiency / assumed rated PF	0.96 / 0.88	pu / pu
Rated current / impedance base	517.74 / 7.3599	A / Ω
Referred rotor inductance	3.8655	mH
Stator R / X; rotor R / X	0.025 / 0.115; 0.024 / 0.165	pu
Magnetising reactance	3.15	pu
LRS resistance limits	0.310 / 0.009	pu
Inertia / viscous damping	3100 / 14	$kg\cdot m^2$ / N·m·s
Electrode time constant / max travel	1.45 / 0.062	s / s^{-1}
Thermal capacity / cooling time	3.8 / 850	$MJ\cdot °C^{-1}$ / s
Maximum α / effective-C ceiling	0.72 / 225	pu / mF
Compensation slip window	$0.18 < s < 0.96$	pu
Current / temperature trip threshold	2.60 / 69	pu / °C
Time step / simulated duration	0.08 / 48	s / s
Performance averaging interval	4-36	s

5. Explicit PSO-Tuned Zero-Order Sugeno Fuzzy Supervisor

5.1 Membership functions, rule firing and inference

The supervisor is a zero-order Sugeno fuzzy controller with three slip memberships and fixed scalar rule consequents. It is not claimed to be a trained ANFIS. The PSO adjusts six interpretable parameters offline, whereas online evaluation uses Gaussian membership functions, normalised firing strengths, a power-factor error and two safety penalties.

$\mu_i(s) = \exp[-(s - c_i)^2/(2\sigma^2)], \quad i \in \{low, mid, high\}$ (21)

$c_l = \max(0.18, c_m - 0.30), \quad c_h = \min(0.95, c_m + 0.30)$ (22)

$\bar{w}_i = \mu_i/(\mu low + \mu mid + \mu high + 10^{-12})$ (23)

$F(s) = 0.23\bar{w}low + 1.00\bar{w}mid + 0.68\bar{w}high$ (24)

$ePF = \max(0.95 - PFdisp, 0)$ (25)

$\alpha raw = 2.55g\ ePF\ F(s) - kI[I_s - Isafe]_+ - kT[T - 53]_+$ (26)

$\alpha^* = sat(\alpha raw, 0, 0.72), \quad Ceff = Cres/\alpha^* \quad$ when the branch is enabled (27)

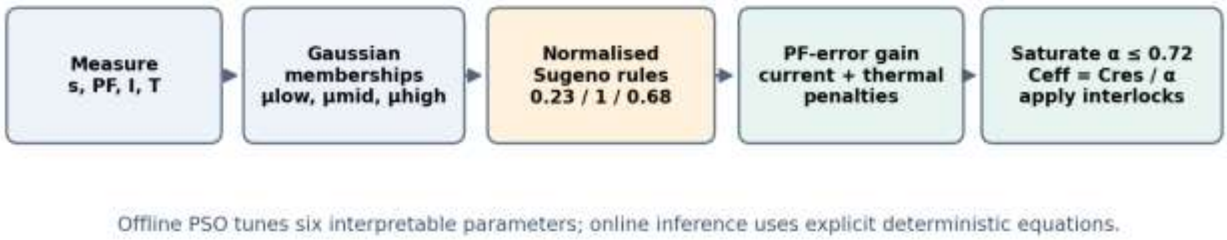

Figure 2. Explicit zero-order Sugeno inference, PSO-tuned parameters and independent safety saturation.

The low-slip rule deliberately requests less compensation because effective capacitance rises sharply as slip decreases. The medium-slip rule receives the largest consequent, while the high-slip rule provides moderate cancellation during early acceleration. Current and electrolyte-temperature penalties reduce the command before the independent trip layer is reached.

Table 3. Fully specified interpretable fuzzy rules and independent permissives.

Rule	Measured condition	Defined controller action
1	Slip is low	Consequent 0.23; prepare branch removal
2	Slip is medium	Consequent 1.00; maximise permitted benefit
3	Slip is high	Consequent 0.68; apply moderate compensation
4	Current exceeds tuned safe threshold	Subtract kI(I - Isafe) and retain trip interlock
5	Temperature exceeds 53 °C	Subtract kT(T - 53) and retain thermal trip
6	Slip/Ceff window or permissive invalid	Disconnect capacitor branch; α = 0

5.2 Coordinated electrode scheduling

$\omega ref,pu(t) = \min(t/35, 0.97), \quad e\omega = \omega ref,pu - \omega pu$ (28)

$$x^* = \mathrm{sat}[t/37 + 0.13e\omega + 0.018\int e\omega dt + 0.045(1 - \kappa c), 0,1] \quad (29)$$

The integral state uses one-sided anti-windup and is bounded from 0 to 8 pu·s; negative accumulation is prevented so that final electrode closure and rotor bypass cannot be blocked by early speed-reference overshoot. Conventional and fixed-capacitor baselines use only the timed electrode ramp. Both untuned and PSO-tuned fuzzy configurations use the same adaptive electrode equation; consequently, the comparison between those two cases isolates the benefit of optimising the six fuzzy parameters.

5.3 Offline particle swarm search and independent repeatability

$$v_i(k+1) = \omega(k)v_i(k) + 1.42r_1(p_i - z_i) + 1.48r_2(gbest - z_i) \quad (30)$$

$$z_i(k+1) = \mathrm{clip}[z_i(k) + v_i(k+1), zmin, zmax] \quad (31)$$

$$Jmax = 4PFavg + 0.65PFmin - 0.72Qavg - 0.70[Ipk - 2.35]_+^2 \quad (32)$$

$$- 0.012E_{LRS,MJ} - 0.006t_{95} - 0.045\alpha pk \quad (33)$$

The objective coefficients are explicitly selected engineering preference weights, not statistically estimated constants or universally valid economic prices. The largest coefficient prioritises mean starting displacement power factor; the minimum-PF and reactive-power terms discourage improvement concentrated at isolated instants; the energy and starting-time terms retain comparable influence for quantities expressed in MJ and seconds; and the compensation term favours restraint. Because these terms have different physical units, their numerical coefficients are meaningful only for the stated bases and model. A deployment should rescale and reselect them against measured feeder capacity, allowable start duration, thermal duty and equipment cost, followed by objective-weight sensitivity or Pareto-front analysis.

The overcurrent term is a soft contingency penalty above 2.35 pu; it is distinct from the independent 2.60 pu trip permissive. The realised peak currents are approximately 1.87 pu, so this penalty is inactive for the reported operating cases and cannot be presented as an experimentally demonstrated current-shaping benefit. A future safety-critical optimisation should assess an active operating-current target, constraint enforcement and worst-case fault conditions separately.

The training condition is the conductivity-drift scenario only; nominal and combined-stress scenarios are held out from optimisation. Each run uses 12 particles, 16 iterations, inertia decreasing linearly from 0.82 to 0.45, velocity clipping at ±22% of each parameter range and a deterministic NumPy random generator. Independent random seeds are 20260818 through 20260829. The best solution was generated with seed 20260824. No fabricated additional Monte Carlo, experimental or hardware data are represented.

Table 4. Search bounds, independently defined untuned baseline and best PSO-tuned parameters.

Parameter	Lower	Upper	Untuned	PSO tuned
Compensation gain g	0.700	3.800	1.3000	3.8000
Medium-slip membership centre cm	0.350	0.760	0.5600	0.3500
Common membership width σ	0.150	0.520	0.2200	0.5200
Safe-current threshold Isafe	1.450	2.250	1.7600	1.4500
Current penalty kI	0.080	0.900	0.3800	0.4967
Temperature penalty kT	0.004	0.070	0.0260	0.0171

Across 12 independent runs, the training objective mean is 2.695520, sample standard deviation is 0.001716, minimum is 2.690429 and maximum is 2.696476. These values demonstrate repeatability for the specified deterministic model, not statistical generalisation to real plants.

Interpretation of Table 4 must remain explicitly conditional on the selected feasible box: the reported gain reaches its upper bound, the medium-slip membership centre reaches its lower bound, the membership width reaches its upper bound, and the safe-current threshold reaches its lower bound. The result is therefore the best observed bounded design for this objective and search space, not an interior optimum, proof of convergence to a global optimum, or evidence that wider bounds are physically permissible. Bound expansion, parameter regularisation and sensitivity analysis require separate justified reruns; no such unperformed reruns are claimed here.

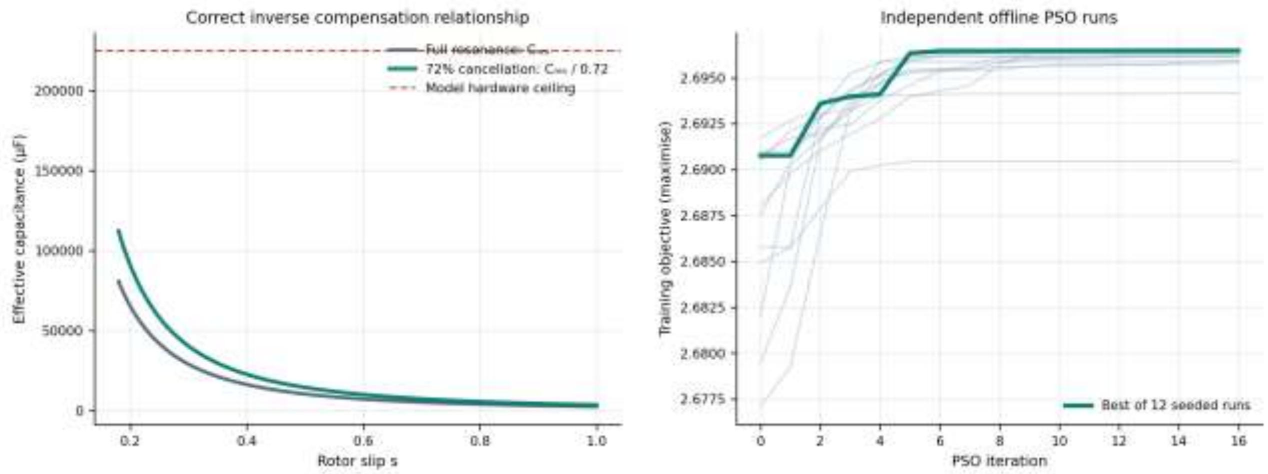

Figure 3. Corrected inverse capacitance relationship and independently seeded PSO convergence histories.

6. Numerical Study Design and Fair Baselines

6.1 Controller definitions and shared safety envelope

Four configurations are compared using identical machine parameters, feeder model, initial conditions, time step, scenario definitions and $\alpha \leq 0.72$ constraint. Controller A is conventional LRS with timed electrode travel and no capacitor. Controller B uses timed electrode travel and a genuinely fixed effective capacitance selected through an independent 33-point grid search on the same training scenario and performance objective. Controller C is the adaptive-electrode Sugeno fuzzy controller with explicitly stated untuned parameters. Controller D is the same fuzzy architecture with offline PSO-optimised parameters.

$$\alpha_{fixed}(s) = \alpha_0(s_0/s)^2, \quad s_0 = 0.55, \quad \alpha_0 = 0.3400 \tag{34}$$

Because a fixed physical capacitance has a fixed capacitive reactance only at one frequency, its compensation fraction changes as $1/s^2$. The fixed-capacitor branch is disconnected when its natural α exceeds 0.72; it is not artificially clipped into behaving like an adaptive capacitor. This treatment gives the fixed comparator an independently selected design point while applying the same safe cancellation ceiling to every compensated controller.

The idealised fixed-capacitor isolation is a fundamental-frequency control decision; contactor opening transients, residual capacitor charge, restrikes and reconnect chatter are not represented. Physical implementation would require an appropriately rated switching device, discharge or precharge circuitry, switching-state confirmation, hysteresis, minimum dwell time and a transient study before the branch can be safely re-enabled.

Table 5. Training and held-out test scenarios with fully disclosed disturbances.

Scenario	Conductivity	Ambient °C	Load factor	Applied condition	Role
Nominal	1.00	35	1.00	Quadratic load only	Held-out test
Conductivity drift	0.84	39	1.04	Two steps + 0.16 Hz oscillation	Training
Combined stress	0.70	43	1.09	Two steps + 0.16 Hz oscillation	Held-out test

6.2 Metrics and reproducibility boundaries

$$PF_{avg} = (1/N)\Sigma PF_{disp}(k), \quad Q_{avg} = (1/N)\Sigma Q_{pu}(k), \quad t \in [4,36]\ s \tag{35}$$

$$\Delta PF_{relative}(\%) = 100(PF_{proposed} - PF_{baseline})/PF_{baseline} \tag{36}$$

$$Q_{reduction}(\%) = 100(Q_{baseline} - Q_{proposed})/Q_{baseline} \tag{37}$$

$$E_{LRS} = \int P_{LRS}dt, \quad IAE_\omega = \int|\omega_{ref,pu} - \omega_{pu}|dt \tag{38}$$

The numerical implementation uses explicit forward-Euler state updates with 0.08 s steps for 48 s. All quantities, scenarios, seeds, controller equations, PSO bounds and load disturbances are given in Sections 4-6 and Appendix A. Reproducibility here means reconstruction of the disclosed reduced-order calculation, not access to proprietary manufacturer data or evidence of experimental replication.

Implementation ordering is material: at each sample the previous-step current and power factor enter the permissive and fuzzy calculation; the electrode position is updated before the rotor impedance; the desired compensation state changes by at most ±0.085 per 0.08 s sample (1.0625 pu/s); commands below 0.075 are disabled; and a violated 225 mF ceiling clears both the applied compensation and its stored state. For input-impedance magnitude $|Z_{in}|$, the current-dependent feeder closure is $V = 1$ when $1/|Z_{in}| \leq 1$, otherwise $V = (1 + k_{grid})/(1 + k_{grid}/|Z_{in}|)$, followed by the declared minimum-voltage clamp. Electrical quantities are then evaluated before forward-Euler thermal and mechanical updates.

7. Results

7.1 Held-out combined-stress starting dynamics

Figure 4 compares the four controllers in the held-out combined-stress condition: conductivity 0.70 pu, ambient temperature 43 °C, load factor 1.09, two load steps and a 0.16 Hz torque disturbance. Conventional LRS yields mean starting PF 0.8506; the optimised fixed capacitor gives 0.8574; untuned Sugeno fuzzy control gives 0.8542; and PSO-tuned Sugeno supervision gives 0.8662. The proposed value differs from conventional LRS by +0.0156 absolute PF units, or +1.84% relative.

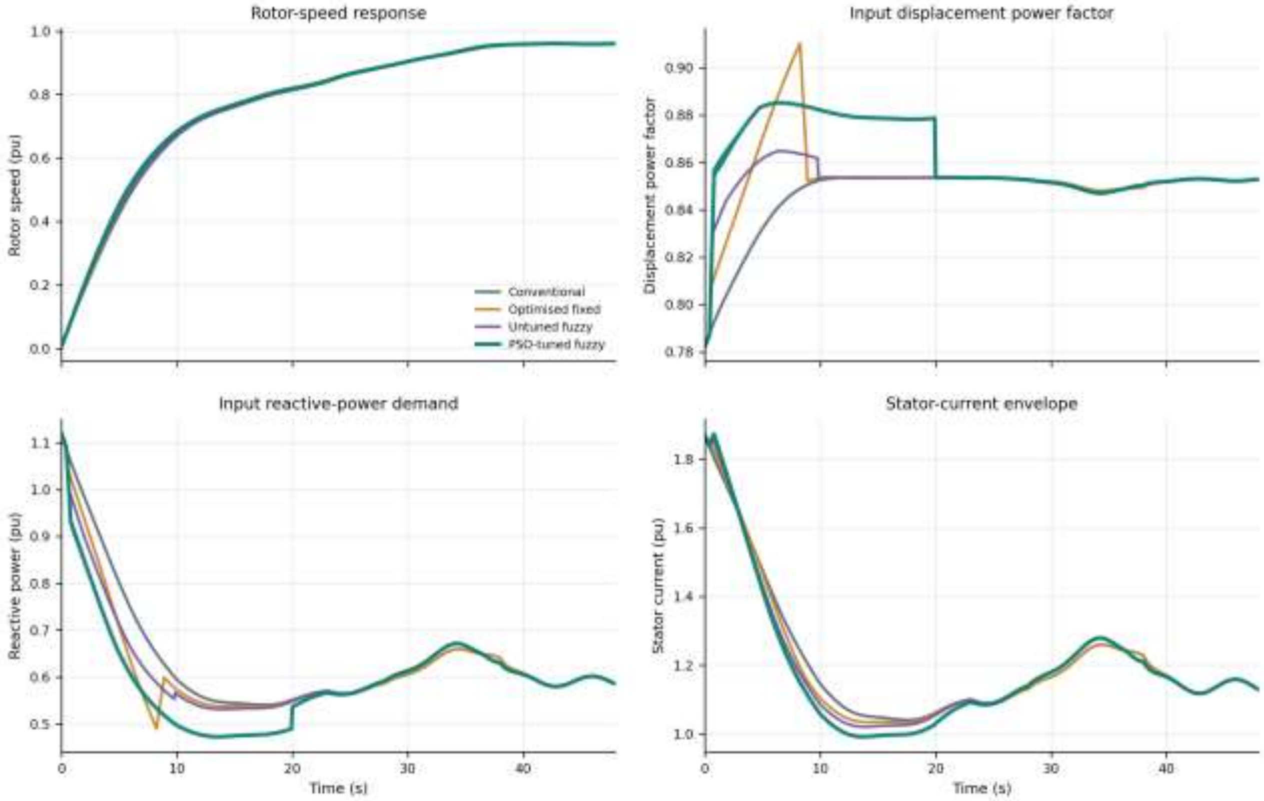

Figure 4. Held-out combined-stress rotor speed, starting displacement power factor, reactive power and stator current.

Mean reactive demand changes from 0.6051 pu for conventional starting to 0.5597 pu for PSO-tuned fuzzy supervision, representing 7.51% reduction relative to the uncompensated baseline. Relative to the independently optimised fixed capacitor, the corresponding reactive-demand change is 4.19%.

7.2 Four-controller performance and explicit trade-offs

Table 6. Recomputed combined-stress results under identical motor, network and safety assumptions.

Performance quantity	LRS only	Optimised fixed	Untuned fuzzy	PSO-tuned fuzzy
Average starting displacement PF	0.8506	0.8574	0.8542	0.8662
Minimum starting displacement PF	0.8240	0.8481	0.8470	0.8470
Average reactive power (pu)	0.6051	0.5841	0.5897	0.5597
Peak stator current (pu)	1.8683	1.8683	1.8694	1.8736
Time to 0.95 pu speed (s)	36.96	36.96	36.32	36.32
Minimum motor-bus voltage (pu)	0.9609	0.9609	0.9609	0.9607
LRS dissipated energy (MJ)	59.52	59.51	59.83	59.74

Performance quantity	LRS only	Optimised fixed	Untuned fuzzy	PSO-tuned fuzzy
Maximum electrolyte temperature (°C)	59.38	59.38	59.46	59.43
Peak reactance cancellation α	0.0000	0.7173	0.2737	0.4297
Minimum resonance margin 1-α	1.0000	0.2827	0.7263	0.5703
Peak effective capacitance (μF)	0	169,034	220,331	224,923
Speed-tracking IAE (pu·s)	7.646	7.830	7.671	7.832

The proposed controller changes peak stator current by +0.28% and integrated LRS energy by +0.36% relative to conventional starting. These results are reported even when they are unfavourable: improved displacement power factor must not be equated automatically with lower starting current, lower electrolyte heating, improved total efficiency or lower whole-plant electrical demand. Protection coordination and starter thermal duty must be evaluated separately [2], [3], [16].

7.3 Compensation, capacitance and thermal trajectories

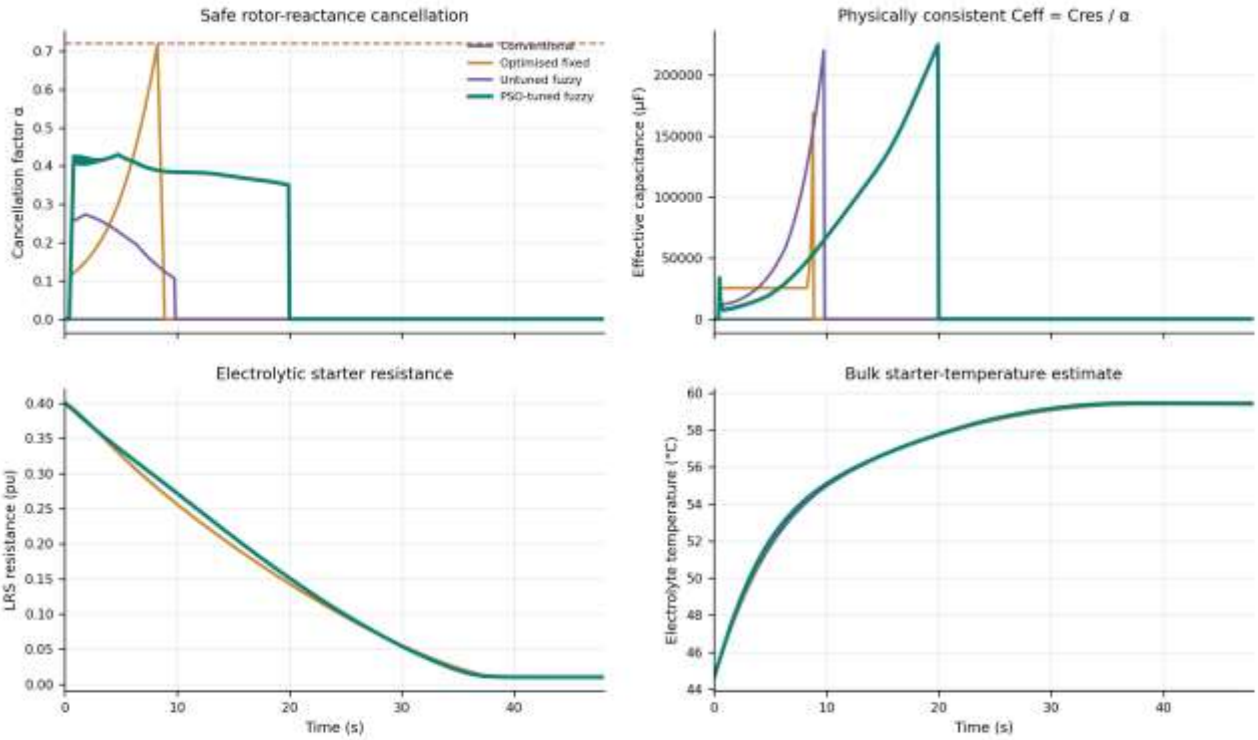

Figure 5. Four-controller compensation factor, corrected effective capacitance, LRS resistance and tank temperature.

The proposed controller reaches peak α = 0.4297, preserving a minimum residual-reactance margin of 0.5703. Its largest enabled effective capacitance is 224,923 μF, below the explicitly modelled 225,000 μF ceiling. The limit is an assumed screening constraint, not a verified converter rating. The fixed-capacitor case is isolated rather than silently converted into a variable capacitor when its safe α ceiling would otherwise be exceeded.

The capacitance headroom is only 76.7 µF, equivalent to 0.034% of the assumed ceiling. Consequently, the reported operating point is practically ceiling-limited: component tolerance, temperature drift, estimation error and converter implementation could trigger earlier disconnection. Section 7.6 therefore quantifies the effect of changing the assumed screening ceiling without retuning the controller.

7.4 Training and held-out scenario comparison

Table 7. Starting power factor across the training scenario and two held-out operating conditions.

Scenario	LRS PF	Fixed PF	Untuned PF	PSO PF	Q reduction
Nominal	0.8486	0.8555	0.8537	0.8620	8.46%
Conductivity drift	0.8498	0.8565	0.8546	0.8652	8.21%
Combined stress	0.8506	0.8574	0.8542	0.8662	7.51%

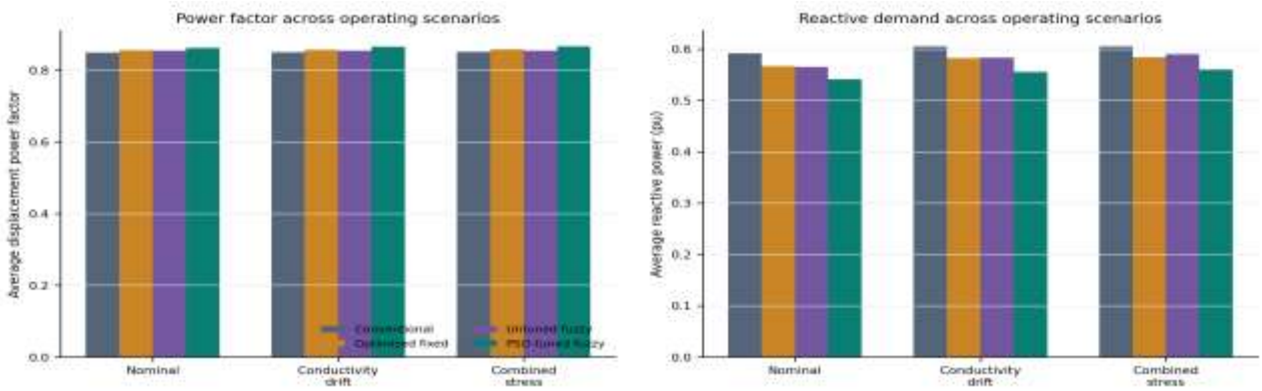

Figure 6. Four-controller starting displacement power factor and reactive demand across all scenarios. The nominal and combined-stress conditions are held-out tests; only the conductivity-drift scenario drives the PSO objective and the fixed-capacitor grid search. This separation reduces training-result leakage, but three deterministic scenarios cannot establish population-level statistical confidence or guarantee behaviour for unmodelled machines.

7.5 Electrolyte-conductivity robustness and PSO repeatability

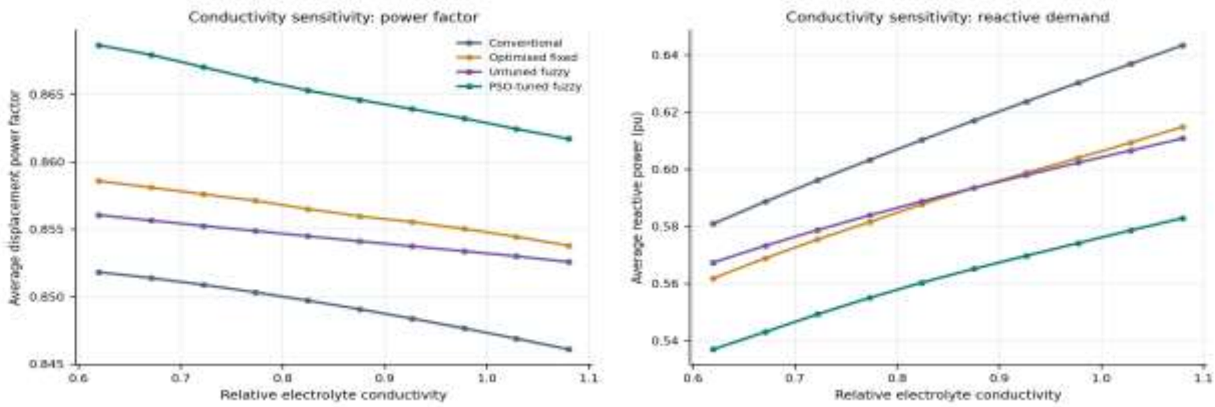

Figure 7. Ten-point conductivity sweep under a common disturbed-load profile.

The sensitivity sweep varies relative electrolyte conductivity from 0.62 to 1.08 using identical 40 °C ambient temperature, 1.06 load factor, torque steps and 0.16 Hz disturbance. The resulting trends demonstrate model-specific sensitivity rather than universal robustness. Sensor noise, rotor asymmetry, actuator backlash, switching harmonics, parameter-identification errors and arbitrary fault combinations are not represented [10], [12].

Table 8. Independent seeded PSO runs: realised objective and selected controller parameters.

Random seed	Objective Jmax	Gain g	Centre cm	Isafe (pu)
20260818	2.696195	3.8000	0.3500	1.5273
20260819	2.694155	3.8000	0.3500	1.7709
20260820	2.696184	3.8000	0.3500	1.5477
20260821	2.696418	3.8000	0.3500	1.5229
20260822	2.696210	3.8000	0.3500	1.5273
20260823	2.696166	3.8000	0.3500	1.5501
20260824	2.696476	3.8000	0.3500	1.4500
20260825	2.695795	3.8000	0.3500	1.4500
20260826	2.690429	3.8000	0.3500	2.2500
20260827	2.695910	3.8000	0.3500	1.4500
20260828	2.695935	3.8000	0.3500	1.4850
20260829	2.696360	3.8000	0.3500	1.4500

The sample mean objective is 2.695520 and sample standard deviation is 0.001716. Objective variation reflects optimisation repeatability for the assumed training condition; it is not a confidence interval for field power-factor improvement. Parameters near a search boundary should motivate a future sensitivity study rather than an unsupported assertion of globally optimal control.

7.6 Effective-capacitance ceiling sensitivity

To test the practical importance of the assumed hardware screen, the unchanged published PSO-tuned controller was actually re-evaluated on the held-out combined-stress condition at five effective-capacitance ceilings. Machine data, controller parameters, scenario, safety limits and integration step were unchanged; the controller was not retuned at each ceiling. Therefore, the comparison isolates sensitivity to the screening limit rather than reporting an unperformed joint converter/controller optimisation.

Table 9. Actual held-out sensitivity to the assumed effective-capacitance screening ceiling.

Ceiling (mF)	Mean PF	Mean Q (pu)	Peak I (pu)	Peak enabled C (mF)
150	0.8633	0.5661	1.8736	149.35

Ceiling (mF)	Mean PF	Mean Q (pu)	Peak I (pu)	Peak enabled C (mF)
175	0.8643	0.5639	1.8736	174.06
200	0.8652	0.5618	1.8736	199.26
225	0.8662	0.5597	1.8736	224.92
250	0.8664	0.5592	1.8736	230.28

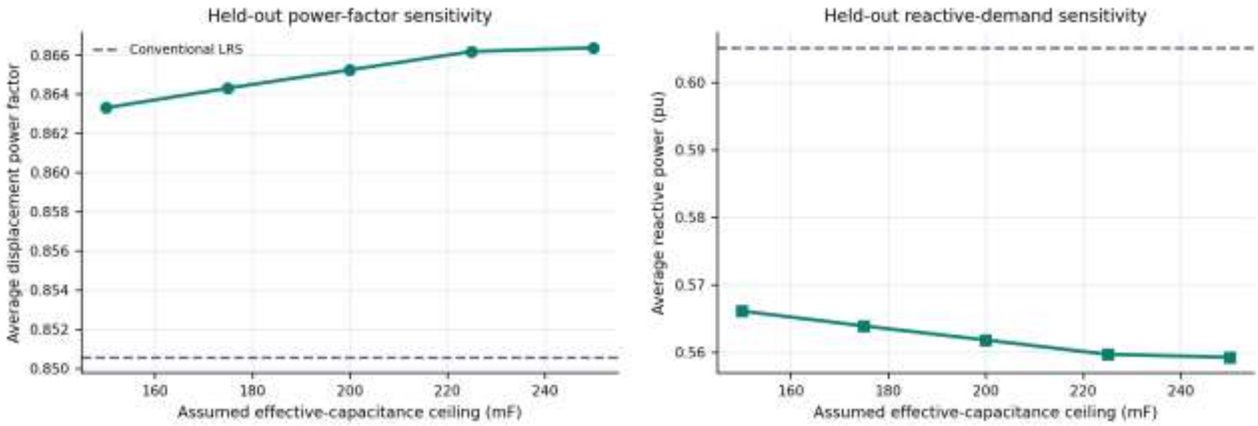

Figure 8. Held-out starting performance versus the assumed effective-capacitance ceiling.

Across the tested 150-250 mF range, held-out mean PF changes from 0.8633 to 0.8664, while mean reactive demand changes from 0.5661 to 0.5592 pu. These are deterministic model results for unchanged controller gains; they neither specify a physical rotor capacitor nor establish manufacturing tolerance, converter rating or industrial feasibility.

7.7 Objective-preference sensitivity among existing PSO candidates

Three engineering-preference profiles were evaluated by rescoring the same twelve independently seeded candidate solutions: PF priority, the published balanced objective, and a thermal/energy-priority preference. For the coefficient vector w = (w_{PFavg}, w_{PFmin}, w_Q, w_E, w_{t95}, w_α), the complete reproducible values are: PF priority w = (5.000, 0.450, 0.500, 0.008, 0.004, 0.025); published balanced w = (4.000, 0.650, 0.720, 0.012, 0.006, 0.045); and thermal/energy priority w = (3.000, 0.650, 0.720, 0.024, 0.010, 0.090). Each score uses $J = w_{PFavg} PF_{avg} + w_{PFmin} PF_{min} - w_Q Q_{avg} - w_E E_{LRS,MJ} - w_{t95} t_{95} - w_\alpha \alpha_{pk} - 0.70[I_{pk} - 2.35]_+^2$. The current contingency remains inactive for the reported candidates and therefore is not described as current-priority optimisation. This is an actual post-hoc candidate-ranking check, not three fresh PSO optimisations and not a complete Pareto-front analysis; each selected candidate is then evaluated on held-out combined stress.

Table 10. Re-ranking of twelve realised PSO candidates under three objective-preference profiles.

Preference profile	Selected seed	Mean PF	Mean Q	Peak I	LRS MJ
PF priority	20260821	0.8672	0.5571	1.8736	59.73
Published balanced	20260824	0.8662	0.5597	1.8736	59.74

Preference profile	Selected seed	Mean PF	Mean Q	Peak I	LRS MJ
Thermal/energy priority	20260824	0.8662	0.5597	1.8736	59.74

A change in selected seed across profiles indicates that the published design depends on explicit engineering preferences; identical or near-identical held-out metrics indicate limited differentiation among the already-generated candidates. Neither outcome removes the need for prospective multi-objective optimisation, physically justified parameter bounds and an active current-limit study before hardware deployment.

8. Industrial Implementation, Protection and Economic Interpretation

8.1 What power-factor improvement does and does not mean

Reducing the net rotor leakage reactance modifies the input impedance angle during the period when the rotor-side compensator is enabled. The reported result is fundamental-frequency motor input displacement power factor during starting. Because the capacitor branch is removed before rotor short-circuit/bypass, the paper makes no claim of persistent running power-factor correction. It also does not claim improvement of an entire plant bus containing other loads or improvement of true power factor when converter-induced harmonics are included.

8.2 Converter topology, physical capacitor rating and insulation

A practical design must begin with the actual standstill rotor line voltage, maximum rotor current, minimum slip at which compensation is enabled, turns ratio, permissible common-mode voltage and insulation coordination. A switched H-bridge or another bidirectional dynamic-capacitance topology must be rated for capacitor ripple current, converter semiconductor current, capacitor voltage reversal, stored energy, snubber dissipation, precharge, discharge and short-circuit fault energy [4], [6].

The stator-referred effective capacitance is not a directly installable physical capacitor bank. An emulated capacitance may differ substantially from the capacitor mounted inside the converter, but no control topology removes the underlying voltage, current, energy or thermal constraints. The duty-to-effective-capacitance map must be derived for the selected topology and verified experimentally before component selection.

Practical design margins must be calculated from measured rotor-side voltage and current rather than inferred from the 225 mF stator-referred screening value. The near-ceiling numerical solution also calls for capacitor-tolerance allowance, thermal derating, sensor-error allowance, worst-case stored-energy calculations and a fail-safe transition to uncompensated LRS operation. These checks are prerequisites for a credible hardware proposal, not evidence already supplied by the reduced-order study.

8.3 Harmonics, EMC and motor-starting studies

The reduced-order model resolves neither converter switching waveforms nor harmonic distortion. Any site design therefore requires an electromagnetic-transient or validated switching model, harmonic assessment at the point of common coupling, rotor-current distortion analysis, common-mode voltage evaluation and EMC verification. IEEE 519-2022 provides a harmonic-control framework, while IEC 61800-3:2022 and its 2025 corrigendum address EMC requirements applicable to power-drive systems [25], [26]. A project-specific motor-starting study must also establish feeder strength, permitted voltage depression and coordination with protective devices [2].

8.4 Independent interlocks, functional safety and hazardous areas

The fuzzy supervisor cannot override independent stator and rotor overcurrent trips, capacitor overvoltage protection, converter overtemperature, electrolyte level and temperature permissives, maximum start-time protection, loss of speed feedback, locked-rotor detection, electrode limit switches, contactor disagreement and emergency shutdown [3], [27], [28]. Compensation isolation must be proven before closing the rotor short-circuit contactor. Safety functions for process applications should be assessed under the applicable IEC 61511 framework rather than being assigned to the non-certified optimisation layer.

Oil-and-gas deployment additionally requires hazardous-area classification, enclosure suitability, cable segregation, inspection, maintenance and project-specific explosive-atmosphere design under IEC 60079-14. Motor rating and performance should be assessed against IEC 60034-1:2026 and the applicable installation documentation [14], [15]. The paper does not imply that the proposed arrangement is already certified for a hazardous area.

8.5 Economic and operational boundaries

Potential operational benefits include lower starting-period reactive demand, improved local feeder utilisation and adaptation to conductivity drift or variable process load. Additional costs include the converter, capacitor, rotor-voltage isolation, sensors, filters, protection interfaces, engineering studies and maintenance. For infrequently started equipment, a conventional starter or carefully selected fixed capacitor may remain preferable. A credible business case must use actual start frequency, process downtime exposure, electrical-network constraints and converter losses; none is inferred from the present model.

9. Limitations and Experimental Validation Roadmap

- The calculation is a deterministic, balanced, fundamental-frequency reduced-order design study; it does not resolve magnetic saturation, spatial harmonics, switching transients, unbalance or converter semiconductor losses.
- The 5 MW motor, network, LRS geometry and thermal parameters are explicitly declared engineering assumptions, not certified or site-measured machine data.
- The control method is an offline PSO-tuned zero-order Sugeno fuzzy supervisor; no trained ANFIS, neural training dataset, hybrid learning validation or machine-learning generalisation guarantee is claimed.
- The physically corrected $C_{eff} = C_{res}/\alpha$ is an effective stator-referred value. The physical converter topology, turns ratio, capacitor rating and experimentally identified duty map remain undefined.
- The four-controller results and twelve PSO runs quantify behaviour only within the stated simulation assumptions; they are neither laboratory measurements nor industrial commissioning evidence.
- The reported performance is starting-period displacement power factor, not continuous-running power factor, total true power factor, measured overall efficiency or whole-plant billing reduction.
- The adaptive-electrode and fuzzy-controller architecture can alter current, bus voltage and LRS thermal duty; a PF benefit does not eliminate those design trade-offs.
- Several tuned parameters terminate exactly at their prescribed bounds; the reported result is only the best observed bounded design. The objective-preference check re-ranks existing solutions but does not replace broader-bound optimisation, regularisation or a full multi-objective sensitivity study.
- The 2.35 pu objective overcurrent penalty is inactive for the approximately 1.87 pu realised peaks, and the effective-capacitance operating point nearly exhausts the assumed 225 mF screening ceiling.

- Ideal branch isolation omits switching transients, residual charge, contactor dwell/hysteresis and semiconductor switching behaviour; these require dedicated electromagnetic-transient and hardware validation.
- No closed-loop global stability proof, independent functional-safety certification, fault-injection campaign or hazardous-area product approval is represented.

Recommended validation proceeds in stages: identify actual stator-referred machine parameters; map LRS resistance against electrode position, concentration and temperature; measure rotor voltage/current across slip; derive and bench-test the selected dynamic-capacitance converter; build a high-fidelity dq/EMT switching model; conduct harmonic, insulation, short-circuit and protection studies; perform controller hardware-in-the-loop and fault-injection tests; validate on an instrumented low-power wound-rotor prototype; and consider an industrial pilot only after independent engineering, functional-safety and hazardous-area approvals [9], [10], [24]-[27].

10. Conclusion

This work presents a physically consistent and transparently bounded approach to improving motor input displacement power factor during the starting of an LRS-equipped slip-ring induction motor. The key correction is $C_{eff} = C_{res}/\alpha$ for partial capacitive reactance cancellation, with branch disconnection at $\alpha = 0$ and a shared ceiling of $\alpha \leq 0.72$. The controller is accurately identified as an offline PSO-tuned zero-order Sugeno fuzzy supervisor rather than an unverified ANFIS.

For the held-out combined-stress numerical scenario, mean starting displacement PF increases from 0.8506 to 0.8662, equivalent to +1.84% relative, and mean reactive demand decreases by 7.51% compared with conventional LRS. Relative to an independently optimised fixed capacitor, reactive demand decreases by 4.19%. The corresponding peak-current and LRS-energy changes are +0.28% and +0.36%, respectively. Twelve explicitly seeded PSO runs provide limited model-level optimisation-repeatability evidence.

Across the five tested 150-250 mF effective-capacitance ceilings, the unchanged controller produces held-out mean PF values from 0.8633 to 0.8664 and mean reactive-demand values from 0.5661 to 0.5592 pu. Preference re-ranking selects seed 20260821 for the PF-priority profile and seed 20260824 for the published balanced profile, confirming that the preferred bounded design depends on the disclosed engineering weights.

The justified conclusion is that safely bounded rotor-side reactance cancellation combined with interpretable PSO-tuned fuzzy supervision merits further investigation for high-power motor starting. It is not yet a proven industrial product. Converter feasibility, harmonic-inclusive true power factor, component thermal duty, safety-rated interlocks, parameter identification and experimental validation remain mandatory before any field implementation.

Acknowledgements

The authors acknowledge their professional affiliation with the Technical and Administrative Training Institute (TATI), Muscat, Oman. The affiliation does not imply institutional sponsorship, industrial-site access or organisational endorsement.

References

1. AOIP, "EPM: Electrolytic starter (LRS) for high-power slip-ring motors," manufacturer technical documentation. Available: https://www.aoip.com/product/electrolytic-starters-for-slipring-motors/epm/
2. IEEE Standards Association, IEEE 3002.7-2018, IEEE Recommended Practice for Conducting Motor-Starting Studies and Analysis of Industrial and Commercial Power Systems, 2018. Available: https://standards.ieee.org/ieee/3002.7/4435/
3. IEEE Standards Association, IEEE 3004.8-2016, IEEE Recommended Practice for Motor Protection in Industrial and Commercial Power Systems, 2016. Available: https://standards.ieee.org/ieee/3004.8/5028/
4. K. Ranjith Kumar, S. Palaniswami and M. Manikandan, "Performance Analysis of Wound Rotor Induction Motor by DSP Based Rotor Dynamic Capacitor Control," Journal of Theoretical and Applied Information Technology, vol. 40, no. 1, pp. 67-77, 2012. Available: https://www.jatit.org/volumes/Vol40No1/10Vol40No1.pdf
5. J. Reinert and M. J. Parsley, "Controlling the speed of an induction motor by resonating the rotor circuit," IEEE Transactions on Industry Applications, vol. 31, pp. 887-891, 1995.
6. C. Suciu, M. Kansara, P. G. Holmes and W. Szabo, "Phase advancing for current in R-L circuits using switched capacitors," Electronics Letters, vol. 35, no. 16, pp. 1296-1297, 1999, doi: 10.1049/el:19990923.
7. J.-S. R. Jang, "ANFIS: Adaptive-network-based fuzzy inference system," IEEE Transactions on Systems, Man, and Cybernetics, vol. 23, no. 3, pp. 665-685, 1993, doi: 10.1109/21.256541.
8. J. Kennedy and R. Eberhart, "Particle swarm optimization," Proceedings of ICNN'95 - International Conference on Neural Networks, vol. 4, pp. 1942-1948, 1995, doi: 10.1109/ICNN.1995.488968.
9. M. Wcislik, K. Suchenia and A. Cyganik, "Vectorized Mathematical Model of a Slip-Ring Induction Motor," Energies, vol. 13, no. 15, art. 4015, 2020, doi: 10.3390/en13154015.
10. S. Bouzid, P. Viarouge and J. Cros, "Real-Time Digital Twin of a Wound Rotor Induction Machine Based on Finite Element Method," Energies, vol. 13, no. 20, art. 5413, 2020, doi: 10.3390/en13205413.
11. U. Sengamalai, G. Anbazhagan, T. M. Thamizh Thentral, P. Vishnuram, T. Khurshaid and S. Kamel, "Three Phase Induction Motor Drive: A Systematic Review on Dynamic Modeling, Parameter Estimation, and Control Schemes," Energies, vol. 15, no. 21, art. 8260, 2022, doi: 10.3390/en15218260.
12. F. J. Basha and K. Somasundaram, "Rotor Asymmetry Detection in Wound Rotor Induction Motor Using Kalman Filter Variants and Investigations on Their Robustness: An Experimental Implementation," Machines, vol. 11, no. 9, art. 910, 2023, doi: 10.3390/machines11090910.
13. F. Beltran-Carbajal, H. Yanez-Badillo, D. Galvan-Perez, I. Rivas-Cambero, D. Sotelo and C. Sotelo, "B-Spline Artificial Neural Networks in Robust Induction Motor Control," IEEE Access, vol. 12, pp. 101679-101700, 2024, doi: 10.1109/ACCESS.2024.3430323.
14. International Electrotechnical Commission, IEC 60034-1:2026, Rotating Electrical Machines - Part 1: Rating and Performance, 2026. Available: https://webstore.iec.ch/en/publication/89961
15. International Electrotechnical Commission, IEC 60079-14:2024, Explosive Atmospheres - Electrical Installation Design, Selection and Installation of Equipment, Including Initial Inspection, 2024. Available: https://webstore.iec.ch/en/publication/66049

16. International Electrotechnical Commission, IEC 60034-2-1:2024, Rotating Electrical Machines - Standard Methods for Determining Losses and Efficiency from Tests, 2024. Available: https://webstore.iec.ch/en/publication/67756
17. MathWorks, "Induction Machine Wound Rotor," Simscape Electrical documentation. Available: https://www.mathworks.com/help/sps/ref/inductionmachinewoundrotor.html
18. Modelica Association, "IM_SlipRing: Model of a three-phase induction machine with slip-ring rotor," Modelica Standard Library 4.0.0. Available: https://doc.modelica.org/Modelica%204.0.0/Resources/helpWSM/Modelica/Modelica.Electrical.Machines.BasicMachines.InductionMachines.IM_SlipRing.html
19. Y. Baghouz and O. T. Tan, "Optimal efficiency speed control of induction motors by variable rotor impedance," IEEE Transactions on Energy Conversion, vol. 4, pp. 216-223, 1989.
20. W. Shepherd and G. R. Slemon, "Rotor impedance control of the wound rotor induction motor," AIEE Transactions, Part III, vol. 78, pp. 807-814, 1959.
21. M. Ayyadurai, B. P. Singh, C. S. Jha and R. Arokiasamy, "On the speed control of wound rotor induction motor using rotor impedance control," IEEE Transactions on Power Apparatus and Systems, vol. PAS-98, no. 5, pp. 1489-1496, 1979.
22. K. Ranjith Kumar and S. Palaniswami, "Performance enhancement of wound rotor induction motor by resonating rotor circuit using fuzzy controller," European Journal of Scientific Research, vol. 52, no. 4, pp. 580-591, 2011.
23. P. C. Sen and K. H. J. Ma, "Rotor chopper control for induction motor drive: TRC strategy," IEEE Transactions on Industry Applications, vol. IA-11, no. 1, pp. 43-49, 1975, doi: 10.1109/TIA.1975.349256.
24. C. J. O'Rourke, M. M. Qasim, M. R. Overlin and J. L. Kirtley, "A Geometric Interpretation of Reference Frames and Transformations: dq0, Clarke, and Park," IEEE Transactions on Energy Conversion, vol. 34, no. 4, pp. 2070-2083, 2019, doi: 10.1109/TEC.2019.2941175.
25. IEEE Standards Association, IEEE 519-2022, IEEE Standard for Harmonic Control in Electric Power Systems, 2022. Available: https://standards.ieee.org/ieee/519/10677/
26. International Electrotechnical Commission, IEC 61800-3:2022, Adjustable Speed Electrical Power Drive Systems - Part 3: EMC Requirements and Specific Test Methods for PDS and Machine Tools, including corrigendum 1:2025. Available: https://webstore.iec.ch/en/publication/65056
27. International Electrotechnical Commission, IEC 61511-1:2016+A1:2017, Functional Safety - Safety Instrumented Systems for the Process Industry Sector - Part 1, consolidated version. Available: https://webstore.iec.ch/en/publication/61289
28. ABB, "R Contactors: Control of AC and DC Power Circuits," technical catalogue, 2015. Available: https://library.e.abb.com/public/c89347ab617a4dc4801b9529978dc2b2/1SXU106047C0201_RContactorsCatalogJuly2015.pdf